Journal of
*Marine Science and Engineering*

MDPI

*Article*

# Validation of a Tool for the Initial Dynamic Design of Mooring Systems for Large Floating Wave Energy Converters

**Jonas Bjerg Thomsen *, Francesco Ferri and Jens Peter Kofoed**

Department of Civil Engineering, Aalborg University, Thomas Manns Vej 23, 9220 Aalborg Ø, Denmark; ff@civil.aau.dk (F.F.); jpk@civil.aau.dk (J.P.K.)

* Correspondence: jbt@civil.aau.dk; Tel.: +45-9940-8552

Received: 11 May 2017; Accepted: 13 September 2017; Published: 22 September 2017

**Abstract:** Mooring of floating wave energy converters is an important topic in renewable research since it highly influences the overall cost of the wave energy converter and thereby the cost of energy. In addition, several wave energy converter failures have been observed due to insufficient mooring systems. When designing these systems, it is necessary to ensure the applicability of the design tool and to establish an understanding of the error between model and prototype. The present paper presents the outcome of an experimental test campaign and construction of a numerical model using the open-source boundary element method code NEMOH and the commercial time-domain mooring analysis tool OrcaFlex. The work used the wind/wave energy converter Floating Power Plant as a case study, which is defined as a large floating structure with a passive mooring system. The investigated mooring consists of a three-legged turret system with synthetic lines, and it was tested for both operational and extreme events. In order to understand the difference between the model and experimental results, no tuning of the model was done, besides adding drag elements with values found from a simplified methodology. This resembles initial design cases where no experimental data are available. Generally good agreement was found for the tensions in the lines when the drag element was applied, with some overestimation of the motions. The main cause of difference was found to be underestimation of linear damping. A model was tested with additional linear damping, and it illustrated that a final analysis needs to use experimental data to achieve the best results. However, the analyses showed that the investigated model can be used without tuning in initial investigations of mooring systems, and it is expected that this approach can be applied to other similar systems.

**Keywords:** wave energy; mooring; numerical; NEMOH; OrcaFlex; validation

## 1. Introduction

During the last few decades, the large focus on renewable energy sources has led to the suggestion of many different types of devices for harvesting energy. A number of these are wave energy converters (WECs), which use different principles for harvesting wave energy. Despite the comprehensive research, the wave energy sector is still not in a commercial state, and above all, there is a need to reduce the levelized cost of energy (LCOE). WECs vary greatly in size and structure, with some of the devices considered as being large floating structures. These form the basis for the present study, with examples of such structures being the Floating Power Plant [1], KNSwing, LEANCON Wave Energy [2] and Wave Dragon [3]. Naturally, floating structures like these need a system to ensure station keeping, which is often solved by using mooring systems. Based on the working principle of the power take off (PTO) of the WEC, the mooring system can either be considered passive, meaning that it does not take part in the power absorption, or it can be considered active or reactive if it

affects the PTO [4]. Common for the type of structures considered in this study is the use of passive mooring systems.

Moorings highly affect the survivability and cost of floating WECs, since even a partial failure of this system can result in a total loss of the device. In addition, the cost of moorings has proven to take up a large part of the total structural cost [5,6] and is, therefore, vital to investigate and improve in order to lower the LCOE. Despite a large experience in mooring design from other offshore sectors, a large number of the WECs deployed offshore have failed due to insufficient moorings [5]. This can partly be explained by a tendency to apply mooring principles from the traditional oil and gas sector with a catenary system of mooring chains. Studies like, e.g., [7–9] show not only that a chain results in a very stiff system with resulting high loads, but also that there could be a great potential for cost reduction in the application of synthetic lines. As a result of this, the developers of the mentioned WECs now consider this as a relevant mooring solution. Consequently, there is a great need for research into cost and reliability optimization of the moorings. A method must be defined that can be used by similar WECs to make an initial investigation of the mooring response.

In order to secure the survivability of the mooring and structure, the system must be designed to survive in all relevant conditions, and therefore, the design parameters like tensions and motions need to be evaluated. According to standards like, e.g., [10–12], it is particularly important to ensure survival in extreme conditions, which is why extreme conditions are the focus of this research. During these conditions, the PTO of the mentioned WECs will be in safety mode and is, therefore, not necessary to consider in the design. A method to identify the parameters must be established either by use of laboratory experiments or by numerical models. Commonly, a test campaign is initiated to provide data on the motion and tension response of the mooring, which is then used for validation of a numerical model. This allows for tuning of the model so that good agreement between experiments and the numerical model is achieved for the tested sea states, mooring layout and model geometry. For instance, [13] presents a methodology for optimization of the numerical model of a WEC, and a similar one is seen in, e.g., [14,15], which considers floating wind turbine platforms, aims to prove the validity of numerical models and tunes them to available experimental tests. For many early stage WECs, however, experimental data are not available, and there is a need for understanding the mooring system behavior prior to performing tests. It often happens that the WECs experience changes during the design phases, which gives a need for new and expensive tests. It is, therefore, essential to have a model that can be used in initial studies of the potential of different mooring layouts and materials, even without access to experimental data. Where studies like, e.g., [13–15] tune the model to fit the experimental results, the present paper tends to validate a numerical tool according to the definition of validation in [16] and identifies errors and their magnitude without tuning it to experimental work. The focus is put on validating design values such as tensions and to some extent, motions, as these determine the applicability of a certain mooring layout. This should justify the use of an identical procedure for analyzing and designing initial mooring systems for other large floating WECs where no experimental data are available. For the final design, it is still recommended to perform tests and to optimize the model to get a better agreement with experiments. In order to illustrate this, an additional optimized model was produced and compared to the experimental data.

The research uses the Floating Power Plant as a case study, cf. Figure 1. This device combines wind and wave energy absorption and has been undergoing comprehensive research in small-scale tests in laboratories followed by an offshore test campaign with a 37 m-wide model. In future research, two different models will be considered: a 60 m-wide model named P60 and a full-scale 80 m-wide model named P80. This paper will consider the P60 device, illustrated in Figure 1, and the sea states from the expected deployment site at the Belgian coast.

The WEC is constructed from a floating foundation (indicated by red color in Figure 1), a wind turbine and four wave energy absorbers (blue color), which utilizes the principle of pitching bodies.


**Figure 1.** Illustration of the Floating Power Plant P60 device. The red color indicates the foundation, and the blue color indicates the floaters (power take off (PTO)).

The paper uses laboratory experiments performed at The Hydraulic and Coastal Engineering Laboratory at Aalborg University, Denmark, for a structure resembling a simplified model of the Floating Power Plant P60 where the wave energy PTO and wind turbine are discarded. The structure is moored with compliant synthetic lines, and the acquired results are compared to numerical results found by using the open source code NEMOH [17] and the commercial software package OrcaFlex v10.0d (Orcina Ltd., Ulverston, UK) [18].

The paper is structured with five sections including this Introduction. The following section presents the applied method in the laboratory experiments and the numerical model, and it is followed by a section presenting the results from both. Section 4 includes a discussion of the results, and Section 5 will present the conclusions and the discussion of future work.

## 2. Method

This section and its subsections provide an introduction of the method used for modeling of the floating structure and its mooring system. It is followed by a short description of the setup used during the laboratory experiments, and more information, description and analysis of the laboratory experiments can be found in [19].

### *2.1. Design and Modeling of Floating Structures with a Mooring System*

There are different design standards available with requirements and recommendations for the design of mooring systems. Among the most commonly recognized are the DNV-OS-E301 [10], API-RP-2SK [11] and ISO 19901-7:2005 [12]. IEC 62600-10 [20] has been developed for mooring design for marine energy devices, while DNV-OS-J103 [21] deals with the general design of floating wind turbines. The design procedure often requires the evaluation of the extreme response and validation according to the extreme tensions in the mooring lines. A time series of an extreme sea is evaluated and the extremes identified, and the data are fitted to a statistical distribution. The requirements of the motions are not as defined as for the tensions and must be decided based on the given location, umbilical specifications, surrounding structures, etc.

Different methods can be applied for the generation of the desired time series. One method includes the use of experimental tests, which provide highly useful results, but are time consuming and potentially expensive. A design procedure is an iterative process and often implies investigation of many different configurations before the most optimized solution is identified. A more common

approach is to apply numerical models, as these are easier to automatize, more changeable and, hence, much less expensive to use. However, it is necessary to validate that the extremes found in the models resemble realistic values, for which experimental data are used. Model validation against experimental data has been done in [13] for a WEC and by several authors like, e.g., [14,15,22,23] for floating wind turbine platforms, mainly considering waves and not the coupled effect of wind and wave exposure.

Different models can be used when simulating the wave-structure and device response numerically. The most commonly-used models are the Morison approach, the boundary element method (BEM), computational fluid dynamics (CFD) or smooth particle hydrodynamics (SPH). Both CFD and SPH put high demands on the computational effort; hence, BEM or the Morison approach are more often used. Many of these models determine the wave/structure interaction, while additional code is needed to simulate the coupled response of the mooring and structure. The BEM includes the load contribution from diffraction and radiation, while the Morison approach includes drag and inertia. The choice, therefore, depends on the sea states in relation to the structure. Often, the diagram by Chakrabarti [24] is used, cf. Figure 7c.

This study uses a modeling procedure as shown in Figure 2. The open source BEM code NEMOH [17] is applied for the calculation of the wave-structure interaction in the frequency domain, which implies linear potential theory with the assumptions of an inviscid, incompressible and irrotational fluid. In addition, the theory assumes incoming waves with low steepness and also structure motions with small amplitudes [17]. Particularly, the two last assumptions are put under stress for a WEC with compliant mooring in extreme sea conditions.

The output of the BEM code is the first order wave excitation force $F_{exc}(\omega)$, the added mass $A(\omega)$, the radiation damping $B(\omega)$ and the Kochin functions $H(\theta,\omega)$. The latter is used to calculate the second order drift force coefficients using the far field formulation [25] and the code available from [26].

The results from the BEM code are coupled with the dynamic analysis tool OrcaFlex [18], which solves the coupled behavior of the mooring system and floating structure in both the time and frequency domain. The model includes the first order wave excitation force and the second order slowly-varying contribution. In this study, the Newman approximation [27] is applied for the calculation of second order motion, which implies that only the mean drift force, calculated from the first order quantities, is used to calculate the second order response. The OrcaFlex package allows for using the full quadratic transfer functions (QTFs), but this has not been considered in this study. It is stated in [18] that the accuracy of the Newman approximation decreases with shallow water depths and also if the natural frequencies are within the frequencies of the wave spectrum. The latter does not cause any concerns as it will always be attempted to design a floating system to have natural frequencies outside the wave spectrum of the extreme seas. In the present study where very large compliance is applied, this problem is even less considerable.

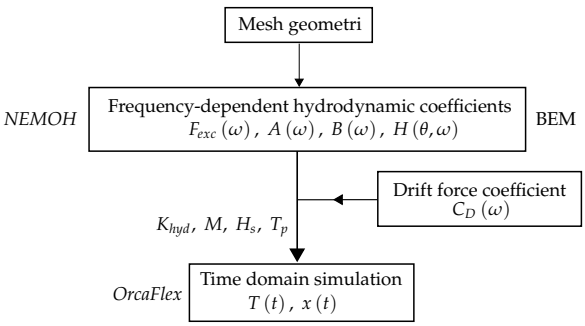


| | |
|---|---|
| $F_{exc}(\omega)$ | Frequency-dependent wave excitation force |
| $A(\omega)$ | Frequencydependent added mass |
| $B(\omega)$ | Frequency-dependent radiation damping |
| $H(\theta,\omega)$ | Frequency- and angle-dependent Kochin function |
| $C_D(\omega)$ | Frequency-dependent mean drift force coefficient |
| $K_{hyd}$ | Structure hydrostatic stiffness matrix |
| $M$ | Structure mass matrix |
| $H_s$ | Significant wave height |
| $T_p$ | Peak wave period |
| $T(t)$ | Time-dependent line tension |
| $x(t)$ | Time-dependent structure motions |

**Figure 2.** Illustration of the numerical modeling procedure used in the present study.

OrcaFlex has the potential to calculate the response using either a radiation/diffraction approach or the Morison approach. It is expected that the use of linear potential theory to include

radiation/diffraction loads will provide a certain level of accuracy, but the drag contribution will be needed, particularly at the resonance frequencies. By combining the two contributions by adding a drag element to the radiation/diffraction calculation, it is possible to obtain a better description. This requires knowledge of the drag coefficient $C_d$, which can either be obtained experimentally or by, e.g., CFD calculations. For cases where this is not possible, a coarse estimate must be suggested.

In order to illustrate the need and effect of this drag element, two configurations were defined for the numerical model:

- Configuration 1: Radiation/diffraction without a drag element.
- Configuration 2: Radiation/diffraction with drag elements in surge, heave and pitch.

The drag coefficients were estimated from a simplified methodology, where the model was divided into a number of simpler shapes (cubes and ellipsoids), as shown in Figure 4e, for which the drag coefficients are known and can be found in, e.g., [28]. The total drag coefficient for the model was then determined by combining the coefficients from each shape, which then provided a very coarse estimate, as it does not account for the interaction between each shape. This methodology does not require the use of experiments or advanced CFD simulations and is, therefore, applicable for initial design.

The numerical model allows for the definition of drag in all degrees of freedom (DoF) by a drag coefficient in the translational DoFs and a drag moment coefficient in the rotational DoFs. The drag moment coefficient was found with respect to the center of gravity using the simplified shapes and corresponding moment arms. The drag coefficients and areas are defined in Table 1.

**Table 1.** Definition of drag coefficients and areas used in the numerical model.

| Parameter | Surge | Heave | Pitch |
|---|---|---|---|
| Drag coefficient, $C_d$ | 1.35 | 1.68 | 1.25 |
| Drag area, $A_d$ | $0.545 \times 10^3$ m$^2$ | $1.92 \times 10^3$ m$^2$ | $7.63 \times 10^6$ m$^5$ |

### 2.2. Experimental Setup

The experiments were conducted in the deep-water basin at The Hydraulic and Coastal Engineering Laboratory at Aalborg University, Denmark, in the period of December 2015–January 2016. The wave basin was equipped with a snake-type wave maker at one end, controlled by the software package AwaSys 7 [29], and a passive absorber at the other end (gravel beach). Five resistant-type wave gauges were used for measurements of surface elevations. The array was located in front of the model, and its layout allowed for 3D reflection analysis. Acquisition, post-processing and analysis of water surface elevation and mooring loads were performed with the software package WaveLab 3 [30] and sampled at a frequency of 123 Hz. The motions of the structure were measured using the OptiTrack system [31], five reflective markers (cf. Figure 4) and four OptiTrack Flex 13 cameras. The Motive 1.9.0 software package was used for data acquisition and analysis.

The choice of scale for the model was based on the specifications of the basin. A range of full-scale sea states and a certain water depth were specified prior to the test campaign, cf. Section 2.2.2. In order to satisfy all conditions, it was found feasible to use a Froude scale of 1:64.5. This corresponds well to the recommendation in [32,33], which states that scale factors of 1:50 and up to 1:80–100 can be used when testing loadings under extreme conditions.

The basin setup is illustrated in Figure 3.

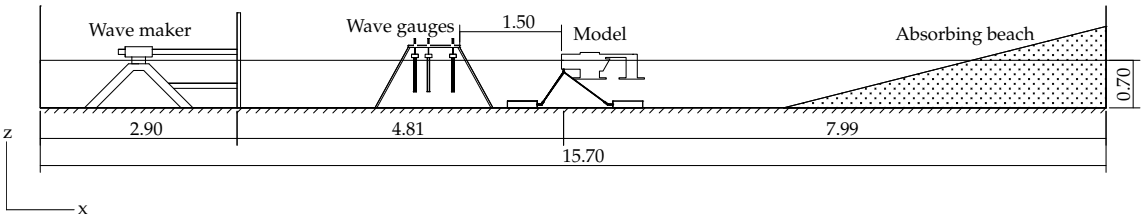


**Figure 3.** Illustration of the experimental setup in the wave basin. All measurements are in m.

The laboratory model resembled a simplified geometry of the Floating Power Plant P60. For simplification, it was decided to discard both the wind turbine and floaters and instead apply their mass at the foundation. In extreme events, it is expected that the loads from wind on the turbine are negligible compared to the wave loads, since the wind turbine will be shut down, and the effective area is much smaller compared to when it is in operational conditions. Despite the large wind speeds, the loads on the structure will be smaller, justifying that the turbine is neglected. Naturally, the position of the turbine mass will affect the mass moment of inertia (MoI), giving larger values. Considering the purpose of validating the numerical model, it is merely important to ensure similarity between the laboratory model and numerical model, hence discarding the wind turbine and floaters do not affect the overall purpose of the study.

Figure 4a,b illustrates the dimensions of the model in full scale, while Figure 4c shows the constructed laboratory model. In the numerical model, the laboratory layout was adapted, and a panel mesh shown in Figure 4d was constructed and analyzed. A convergence analysis was performed in order to justify the number of 1768 panels.

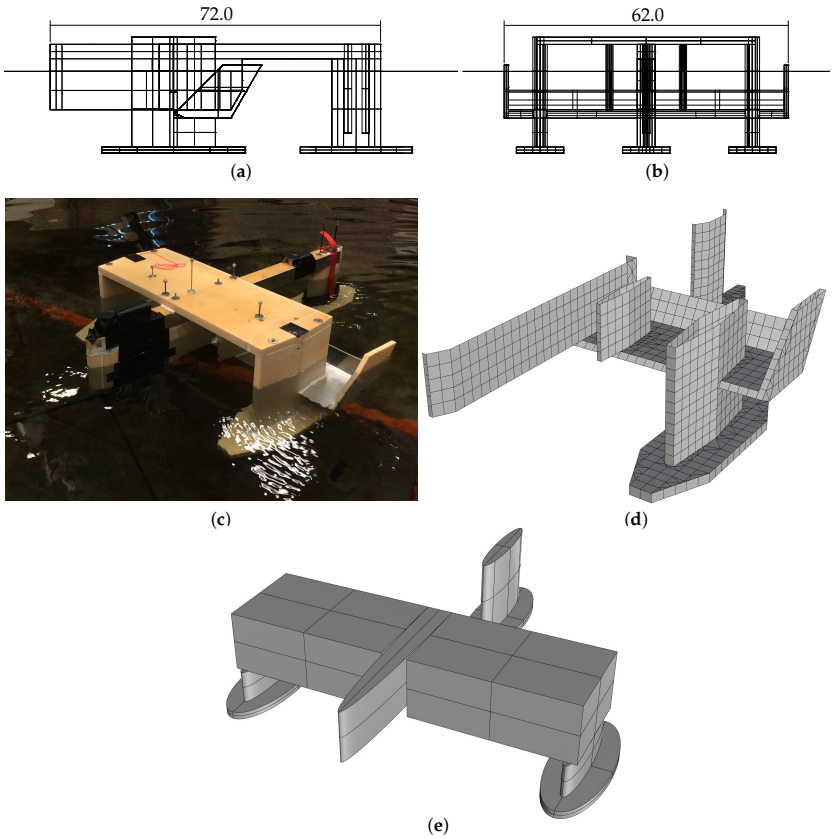


**Figure 4.** (**a**) Side view of the laboratory model at the prototype scale (measurement in m); (**b**) front view of the model; (**c**) picture of the laboratory model; (**d**) illustration of the mesh used in the BEM code; (**e**) simplified geometry used for the estimation of drag coefficients.

The structural parameters of the lab model were measured in the laboratory, and the values were subsequently used in the numerical model. In particular, the model mass and mass moment of inertia (MoI) are of importance in order to model the motion response correctly. Table 2 lists the measured and prototype values.

**Table 2.** Model specification. Note that moment of inertia (MoI) is around the center of gravity.

| Parameter | Model-Scale | Full-Scale |
|---|---|---|
| Structure mass, $m$ (kg) | 22.4 | $6.0 \times 10^6$ |
| Moment of inertia, $I_{xx}$ (m$^2$ kg) | 1.474 | $1.645 \times 10^9$ |
| Moment of inertia, $I_{yy}$ (m$^2$ kg) | 2.525 | $2.819 \times 10^9$ |
| Moment of inertia, $I_{zz}$ (m$^2$ kg) | 3.325 | $3.712 \times 10^9$ |

#### 2.2.1. Mooring System

The mooring was applied as a standard solution with three taut synthetic lines installed as shown in Figure 5a. Despite a different shape of the stiffness curve, the linearized stiffness of the lines corresponds approximately to, e.g., Ø120 mm Bridon Superline Nylon [34]. Three load cells of the type FUTEK LSB210 50/100 lb. were installed at the connection point between the anchor and lines, and a VETEK 30 kg IP68 was positioned at the connection point between the lines and model, cf. Figure 5.

A static test determined the stiffness of the lines where each line was gradually tensioned and the elongation measured. The stiffness curve is plotted in Figure 5b, showing mild non-linearity. The mooring system in the numerical model was defined with the experimentally-measured values of line stiffness and layout. The drag and inertia coefficient of the lines were chosen based on standard values from DNV-OS-E301 [10]. Table 3 provides data on the mooring line characteristics found in the laboratory and applied in the numerical model. No structural damping in the lines was defined in the numerical model, as these values are unknown.

The mooring lines in the numerical model are divided into a number of segments and modeled as straight massless segments. All properties like mass, buoyancy, etc., are lumped to the nodes at each end, while axial and torsional properties are modeled by the segments. A higher number of segments, $n$, generally provides a higher level of accuracy to the model, but is paid by higher computational time. In order to find the number of segments that balances the accuracy and computational time, a convergence analysis was performed and presented in Figure 6 with the number of segments ranging from 5–30. The figure presents the error between the tensions found from each test and the test with the maximum number of segments. A relatively small error is found (less than 1%), and the results clearly converge with $n \geq 15$. The largest error is found for the tension minimums where the lines are slacked. However, the minimum tensions are not of significant importance for the design of moorings, and for $n \geq 15$, the error becomes less than 5%. Based on this, $n = 15$ was used in the numerical model, resulting in a segment length of 3 m.

**Table 3.** Mooring line specifications.

| Parameter | Model-Scale | Full-Scale |
|---|---|---|
| Unstretched length (m) | 0.7 | 46.1 |
| Nominal diameter $d$ (m) | 0.01 | 0.6 |
| Mass (kg/m) | 0.04 | 176.0 |
| Number of segments $n$ (-) | 15 | |
| Segment length (m) | - | 3 |
| Drag coefficients (axial/normal) (-) | 0.0/1.6 | |
| Inertia coefficients (axial/normal) (-) | 0.0/1.0 | |

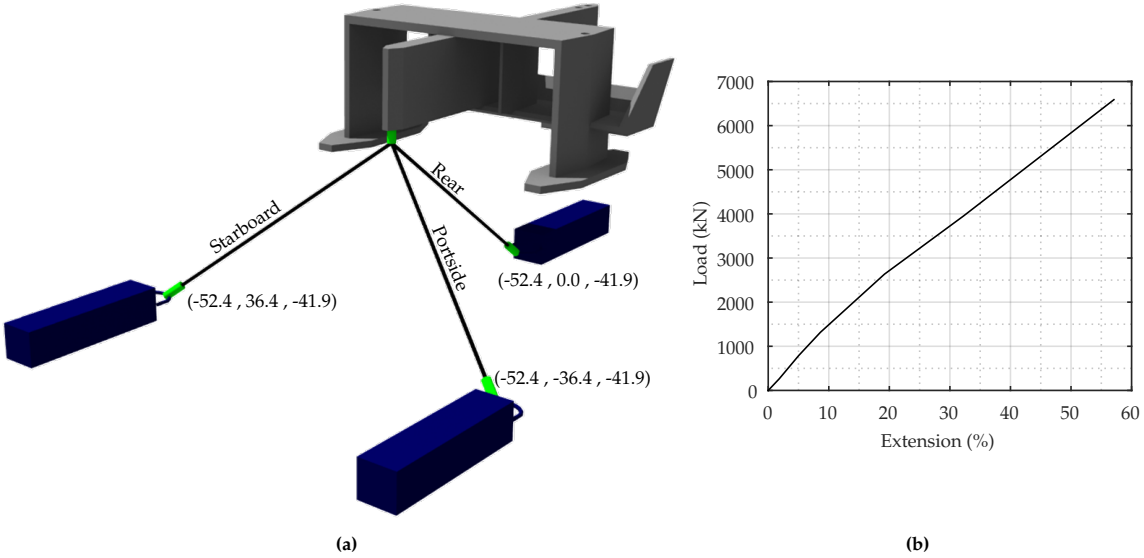


**Figure 5.** (**a**) Illustration of the considered mooring layout. The green shapes illustrate the load cells. (**b**) Mooring line stiffness curve determined during experiments. The values are presented at full scale.

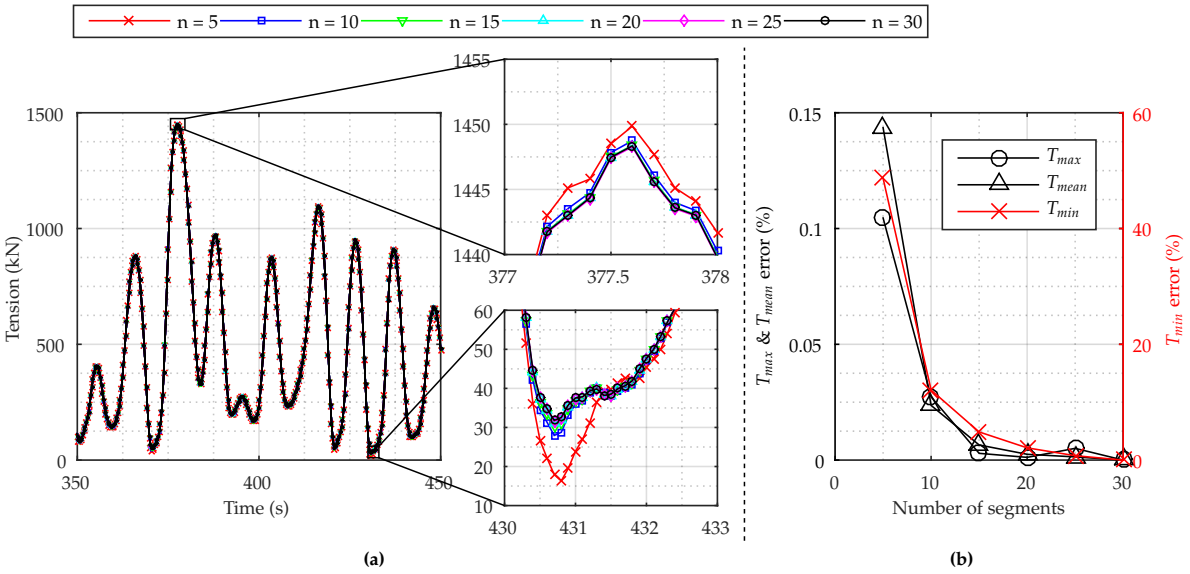


**Figure 6.** (**a**) Time series of segment convergence analysis with a zoom on the maximum and minimum tensions; (**b**) error of each analysis compared to the test with the maximum segment number. Note the different $y$-axes.

The mooring lines were installed with an axial pretension of approximately 315 kN, cf. Figure 8a,b. This tension results from a relatively small extension of the lines (cf. Figure 5b), which caused slacking of the lines during wave exposure.

### 2.2.2. Environmental Conditions

The tested sea states resemble the conditions expected at the deployment site of the P60. Three operational ($H_s$ = 1.3–3.3 m and $T_p$ = 6.4–8.6 s) and six extreme ($H_s$ = 5.1–6.1 m and $T_p$ = 8.6–13.7 s) sea states were tested in order to ensure that the expected range of wave frequencies and wave heights were covered; see Figure 7a. The sea states were simulated as long-crested waves (2D) and with a JONSWAP spectrum (peak enhancement factor $\gamma$ = 3.3). The duration of the individual time

series was determined so that it allowed for a number of 1000 simulated waves according to the recommendations in [33].

In addition to the irregular sea states, 23 regular wave trains were tested. Considering the application areas of wave theories as defined in [35] and plotted in Figure 7b, the *x*-axis shows that the waves primarily will be in intermediate water depths with some of the tested waves in deep water conditions. The *y*-axis indicates the variation of steepness of the waves. It is seen that all sea states can be considered non-linear, hence stressing the assumption of the linear wave potential theory.

As described, the dominating force contribution is highly dependent on the structure diameter in relation to the wavelength. Considering the boundaries defined in [24] and plotted in Figure 7c, it is seen that, when considering the entire structure as one closed body, most of the sea states are in the load regime where diffraction is dominant. For the longest waves, the model will be in a regime where other load contributions have an effect. The investigated structure has a complex geometry where water can pass through the body, which truly does not follow the theory of [24]. Considering, e.g., just the width of each of the vertical columns (cf. Figure 4), the force might be dominated or affected significantly by more than diffraction.

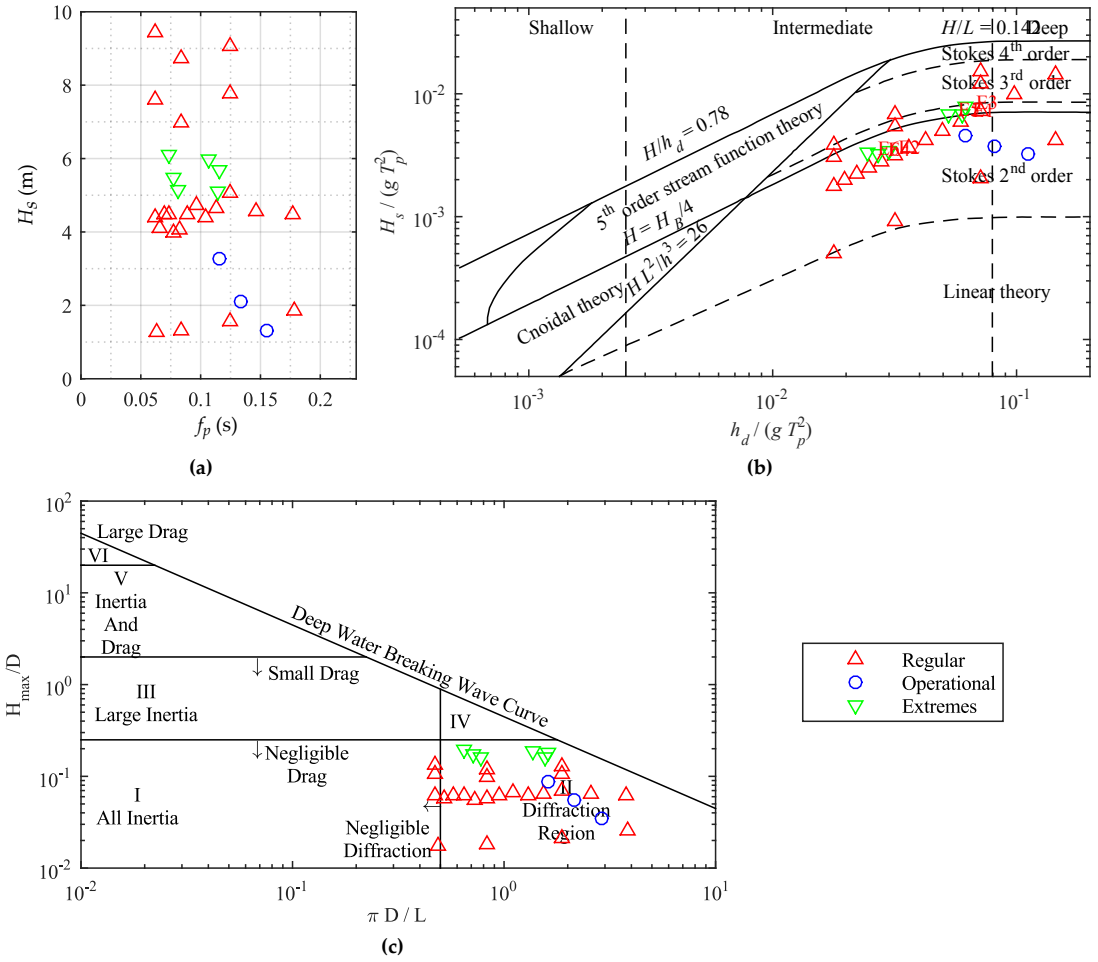


**Figure 7.** (**a**) Diagram of the sea states simulated in the wave basin; (**b**) the sea states plotted against the depth condition (*x*-axis), wave steepness (*y*-axis) and application areas of wave theories as defined in [35]; (**c**) the sea states plotted against wave force regimes as defined in [24], with *D* being the total width of the structure and not considering the open spaces.

## 3. Results

This section presents the results obtained from the numerical model and experimental work. These results will be compared to each other and used to investigate the validity of the numerical model.

### 3.1. Quasi-Static Results

A quasi-static test was carried out for validation of the mooring layout and modeling of line tension. The model was displaced in the surge DoF at a low velocity in order to avoid any dynamic effects. Due to the low velocity, the only restoring force present in the system resulted from the stiffness of the mooring lines. Figure 8a,b plots the measured loads in respectively the starboard and rear mooring line. The experimental results show some scattering of the results, which can be explained by the fact that the model was displaced manually. When the model is displaced, the mooring point will displace vertically as shown in Figure 8c, and this displacement is very sensitive to the physical handling of the model. For a perfect test with no displacement in any other DoF than surge, the scatter would not be expected. Prior to the measurement, one load cell was damaged; therefore, results from the port side line cannot be presented. It would have improved the reliability of the tests since both lines should have shown similar results.

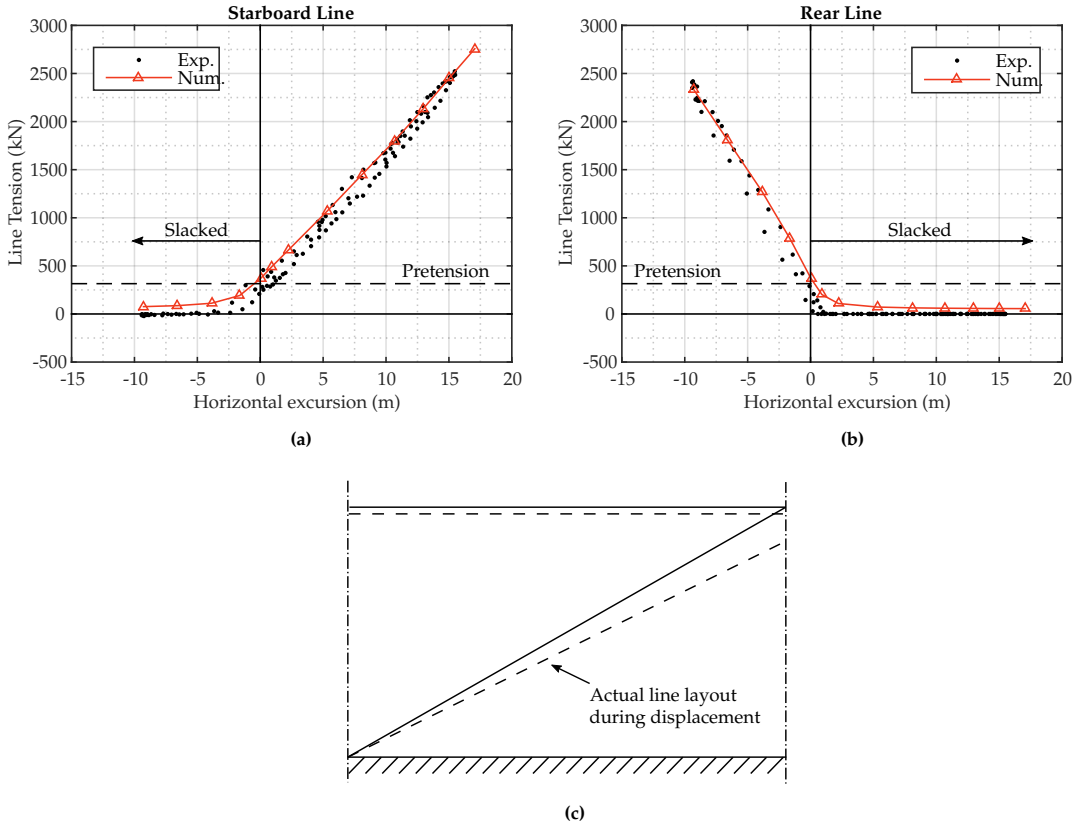


**Figure 8.** Quasi-static test results for experimental (Exp.) and numerical (Num.) line tension in the starboard (**a**) and rear (**b**) line; (**c**) illustration of the line layout during surge motion.

When observing Figure 8, it is seen that the numerical results are within the scatter of the experimental results, and therefore, this illustrates the similarity of the mooring stiffness in the two models. The difference, which is seen to be approximately constant, can be explained by the tactile inaccuracy in the physical handling of the model as described previously. The most dominant difference is seen when the lines are slacked where the numerical tension is higher than the experiments. In the laboratory, no tension was measured in the completely slacked lines, while some tension was found in

the numerical model. This is because the lines are buoyant and give some tension in the connection point. This effect was not seen in the laboratory, possible due to the presence of load cells.

### 3.2. Decay Test

A decay test was used to compare natural frequencies of and damping in the two models. The test is performed by giving a displacement in one DoF, releasing the model and allowing the motion to decay. Due to the complexity of the model, it is difficult to activate only one DoF at a time, and hence, it is difficult to find natural frequencies for all DoF. The test presented a coupled frequency at 0.078 Hz where the structure was activated in surge, heave and pitch. It was possible to activate only the surge DoF in both numerical and experimental tests, even without applying any restraints on the other DoFs. This means that even though the primary motion was in the surge DoF, some motions were also seen in heave and pitch, cf. Figure 9c. Since the scale of the experiments was 1:64.5, the magnitudes of the heave and pith motions are negligible compared to the surge (less than 4 mm in the laboratory). It was not possible to obtain any reliable results for heave and pitch only. The surge decay test is illustrated in Figure 9a for the configurations with and without the drag element.

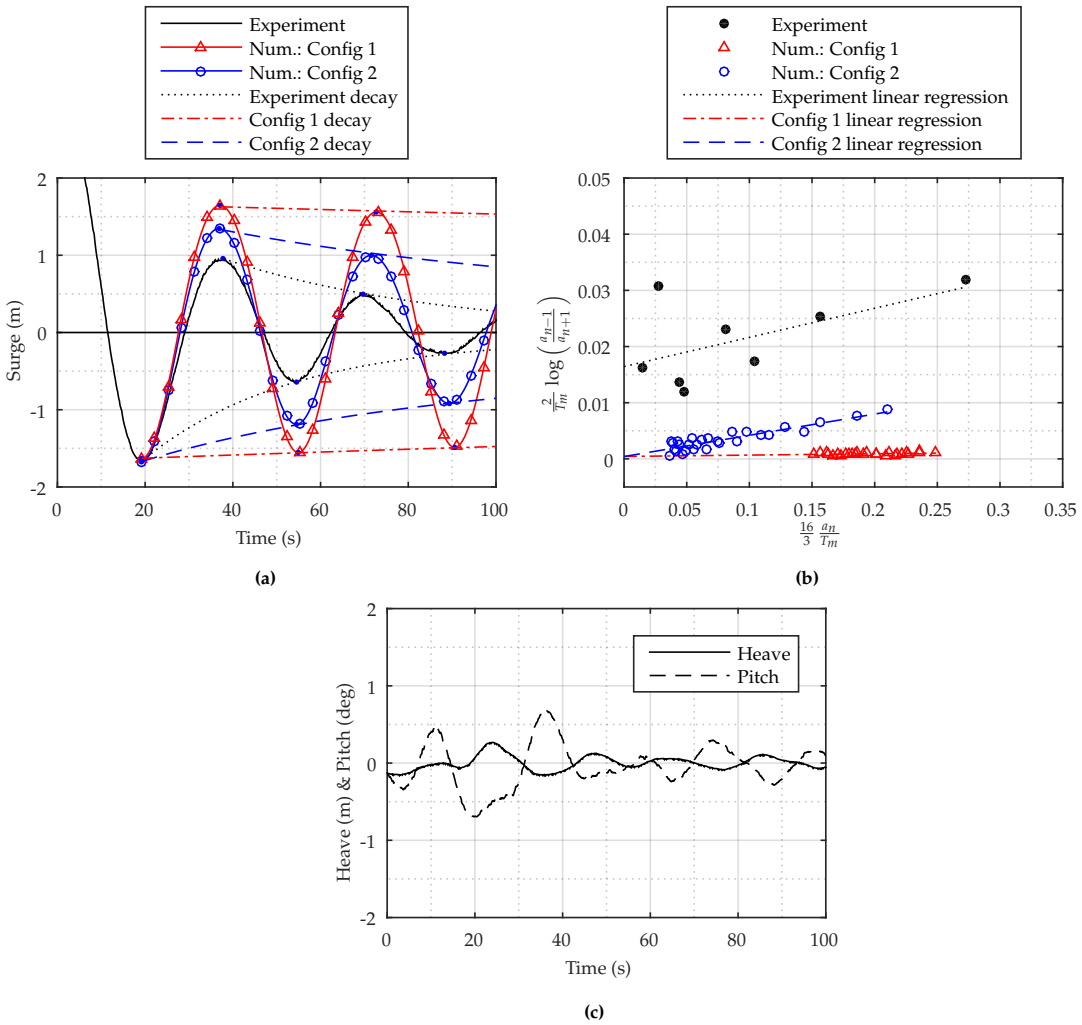


**Figure 9.** (**a**) Free surge decay test from experiments and Configurations 1 and 2 (with and without the drag element); (**b**) determination of linear and quadratic damping coefficients using linear regression [36]; (**c**) heave and pitch motion during the surge decay test.

In the decay test, the structure moves at its natural frequency $f_n$, and the motion is dependent on the structure mass $M$, added mass $A$, radiation damping $B$, hydrostatic stiffness $K_{hyd}$ and mooring stiffness $K_{moor}$.

The peaks and troughs of the motion in Figure 9 were detected and used to calculate the natural frequency as the average of the values. The first oscillation was not considered in order to avoid the influence of releasing the model. Since the structure itself does not provide any hydrostatic stiffness in surge, the natural frequency is mostly dependent on the mass, added mass and mooring stiffness. The mass defined in the numerical model is based on the mass measured in the laboratory and, therefore, does not affect the comparison. When considering the quasi-static test, it was determined that there was good agreement between numerical and experimental stiffness. Therefore, the difference in the two natural frequencies mostly describes any inaccuracies in the calculated added mass in the BEM solver. Considering the results in Table 4, it is however found that the error is approximately 7% for Configuration 1, while it is 4% for Configuration 2, and as such, the results can be considered acceptable.

**Table 4.** Measured and calculated natural frequency, linear and quadratic damping in surge, together with the relative error.

| Parameter | Experiment | Num.: Config 1 Value/Relative Error | Num.: Config 2 Value/Relative Error |
|---|---|---|---|
| Natural surge frequency, $f_n$ | 0.0305 Hz | 0.0284 Hz/6.9% | 0.0293 Hz/3.9% |
| Linear damping, $p_1$ | 0.0164 $s^{-1}$ | 0.0004 $s^{-1}$/97.6% | 0.0004 $s^{-1}$/97.6% |
| Quadratic damping, $p_2$ | 0.0519 $m^{-1}$ | 0.0024 $m^{-1}$/95.4% | 0.0378 $m^{-1}$/27.2% |

The decay test can additionally be used to illustrate the damping of the system, which is the combination of a linear and quadratic contribution. Figure 9 clearly shows that the numerical model highly underestimates this fact, with the largest difference occurring for Configuration 1. In [36], Equation (1) is used to determine the linear and quadratic damping coefficients $p_1$ and $p_2$.

$$\frac{2}{T_m}\log\left(\frac{a_{n-1}}{a_{n+1}}\right) = p_1 + \frac{16}{3}\frac{a_n}{T_m}p_2 \tag{1}$$

where $T_m$ is the natural period and $a_n$ is the amplitude of the $n$-th oscillation. When plotting the left-hand side of the equation against the right-hand side, it is possible to use linear regression to calculate $p_1$ and $p_2$. This is illustrated in Figure 9b, and the results are listed in Table 4. Due to a limited number of oscillations in the experimental decay test, the linear fit is not as good as for the numerical results.

When considering Table 4, it is clear that the numerical model in Configuration 1 highly underestimates the quadratic drag arising from viscous effects. An error of 95.4% is seen, which is reduced to 27.2% in Configuration 2 by adding the drag element. Since no additional linear damping is added to the model, similar results are obtained from the two configurations with a relatively high error of approximately 98%. Section 3.5 presents an optimized model with additional linear damping in order to illustrate its influence on the obtained results.

### 3.3. Regular Sea States

A total of 23 regular sea states were tested (cf. Figure 7a) and used to determine the response amplitude operators (RAOs) for the motions, tensions and the mean drift motion.

#### 3.3.1. Motion Response

The motion was measured in surge, heave and pitch. and their RAOs are plotted in Figure 10, together with the numerical results.

Considering the results from Configuration 1 (Figure 10a–c), there is some agreement with the experiments for most of the frequency range in all DoFs, showing the similar shape and amplitude of the RAOs. Both numerical and experimental RAOs show a peak at the coupled motion frequency at 0.078 Hz, but at this frequency, the most severe difference is observed. Due to resonance motion and lack of damping, most stress is put on the linear potential theory, and the numerical model highly overestimates the motion amplitude. For Configuration 2 (Figure 10d–f) with a drag element in all DoFs, better agreement between the experimental and numerical results is obtained, even at the peak of the RAOs. Still, there is an overestimation, but the error is decreased.

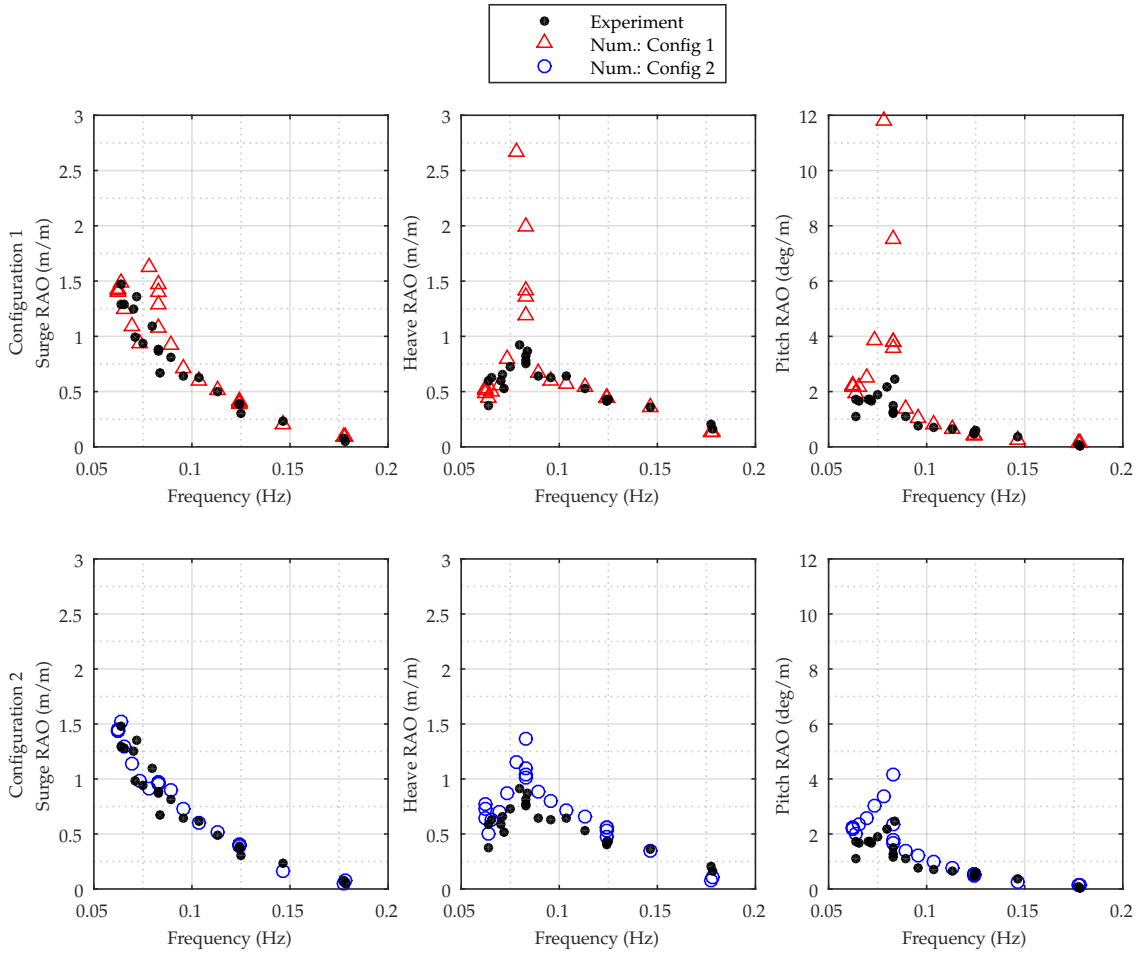


**Figure 10.** Measured and calculated motion response amplitude operators (RAOs) in surge, heave and pitch.

### 3.3.2. Mean Drift

Figure 11 presents the results for the calculated and measured mean drift motion. In the numerical and experimental model, the mean drift during wave exposure is defined as the mean displacement from the static position. Considering the entire frequency range, both over- and under-estimations are seen, and due to the large error in the motion amplitudes at the peak frequency, Configurations 1 provides paramount drift motion errors at this frequency. A very large underestimation is seen with even negative drift, while the drift at the remaining frequencies shows a similar trend as for the experiments. Despite the better resemblance with experiments, Configuration 2 also shows some deviation from the experimental results. Considering Figure 11, it is seen how the drift motion is overestimated at the lowest frequencies and underestimated for many of the higher frequencies, but with a trend following the trend of the results. Despite this error, the motion amplitudes were

shown in Figure 10 to resemble the experiments. Therefore, the error in the drift has proven not to affect the motion amplitude significantly.

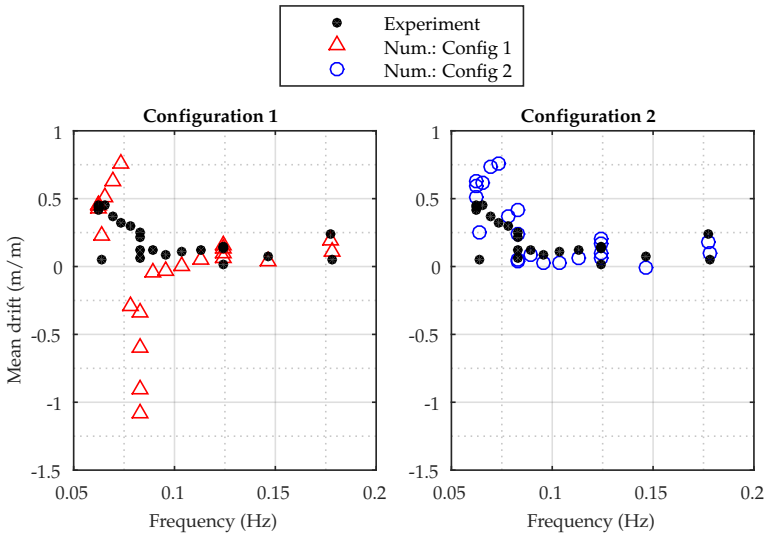


**Figure 11.** Measured and calculated drift motion RAOs for the two configurations.

### 3.3.3. Tension Response

Considering the difference in measured and calculated motion response, especially in the drift motion, some error was expected in the calculated tensions, which are plotted in Figures 12 and 13. Overall, the numerical model shows good agreement with the experiments, but with a high overestimation of the tension around the peak frequencies in Figure 13, a consequence of the high overestimation of the motions. As expected, this is most dominant for Configurations 1 (Figure 13a,c). For the low frequency waves, the tension amplitudes are underestimated, but considering Figure 12, which presents a direct time series comparison between experiments and Configuration 2, the peaks of the tension time series are similar for both models, indicating that the numerical model describes the maximum values well. A difference can be observed between the tension troughs in the figure, which explains the smaller amplitudes.

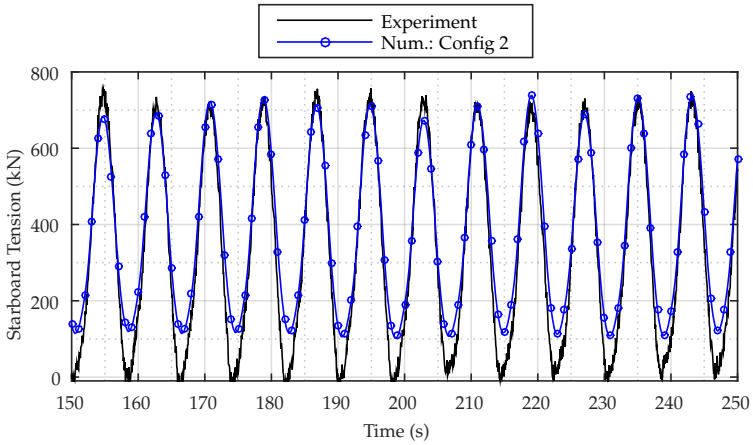


**Figure 12.** Direct comparison of measured and calculated tension time series for a regular sea state with $H = 5.1$ m and $T = 8.0$ s.

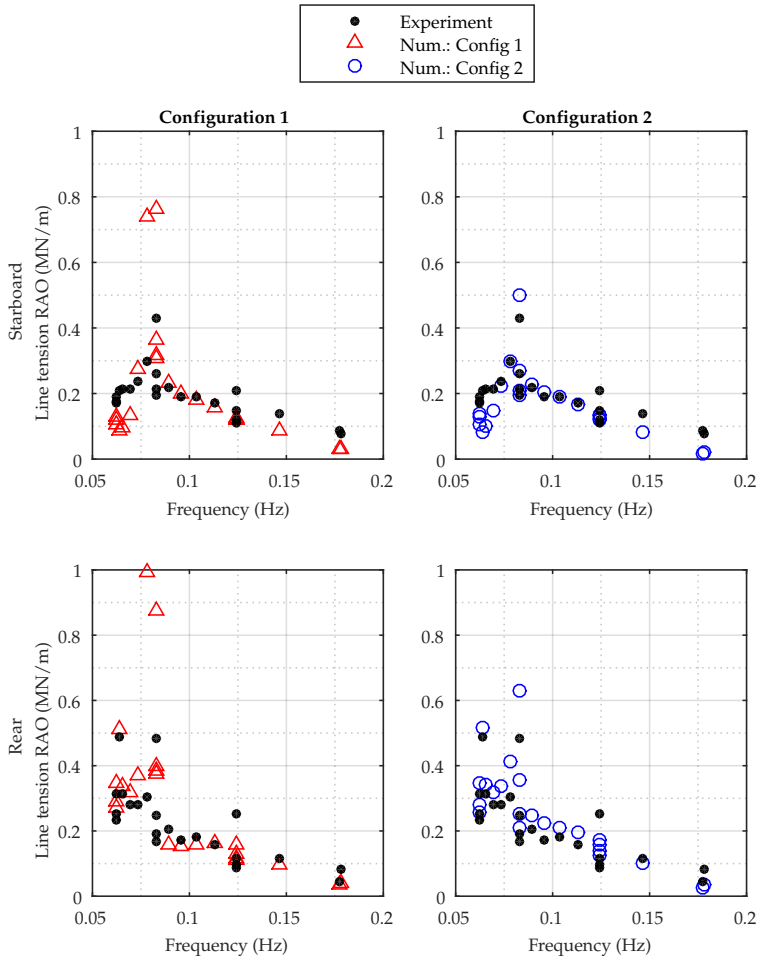


**Figure 13.** Measured and calculated tension RAOs in starboard and rear lines.

### 3.3.4. Influence from Wave Height

As seen in Figure 7a a number of the regular sea states covered a similar wave frequency with varying wave heights in order to investigate non-linearities in the response of the structure. Figure 14 illustrates the motion RAOs and mean drift against the wave height for these experiments and Configuration 2. For the surge DoF, the numerical and experimental results show similar tendencies, but the numerical model overestimates the response. For the shortest waves ($f = 0.12$ Hz), there is good agreement independent of the wave height, but a large error is seen at 0.83 Hz for the lowest wave height. This frequency corresponds to the peak seen in the heave and pitch DoF (cf. Figure 10). The numerical response is seen to be almost linear in surge, but the experiments show a non-linear influence from wave height.

The response in the heave DoF illustrates non-linearity, and it is highly influenced by the wave frequencies. The tendencies found in the experiments and the numerical model are similar, and the magnitude of the difference seems independent of the wave height. A similar observation is found for the pitch DoF, with good agreement for the shortest waves where the smallest motions are present. More dominant errors are found at the natural frequency and for the longest waves where a large response will occur.

The figure clearly indicates that the calculated RAOs are highly influenced by the incoming wave height, and not linearly dependent on it. The magnitude of the deviation between numerical and experimental results seems more dependent on wave frequency than wave height.

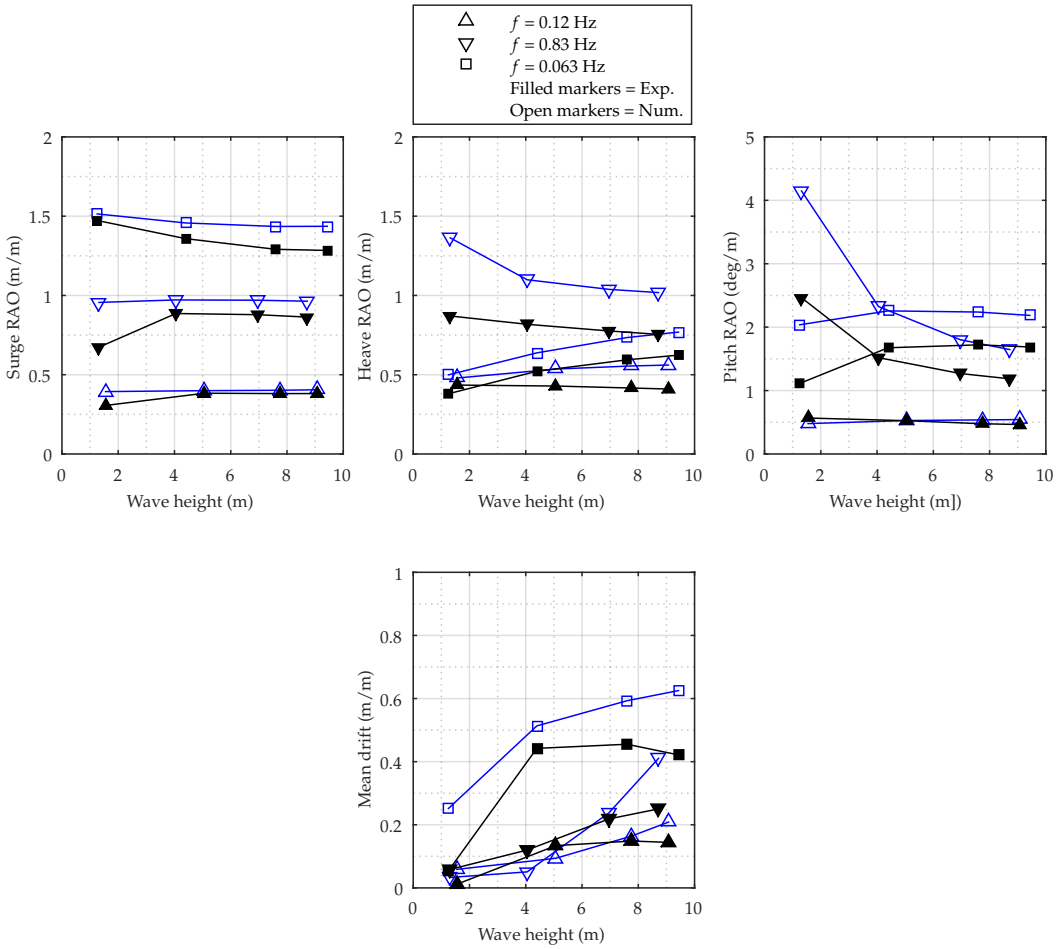


**Figure 14.** Experimental and numerical RAOs for varying wave heights.

### 3.4. Irregular Sea States

The extreme values of the irregular sea states were found and presented in Figures 15 and 16. In this study, the maximum simulated and measured value is considered together with the most probable maximum, cf. Equation (2), which is commonly used for design in, e.g., [10].

$$T_{MPM} = \mu + \sigma\sqrt{2\ \ln(N)} \tag{2}$$

where $T_{MPM}$ is the most probable maximum (MPM) tension in $N$ waves, $\mu$ is the mean tension and $\sigma$ is the standard deviation. This study uses the MPM value in 1000 waves.

Since the numerical and experimental wave time series are not identical, but have similar frequency domain parameters, it is not possible to compare the maximum values directly. Considering Figure 15, there is good agreement in both configurations for the two tests with highest peak frequencies (operational conditions). These also have the smallest wave height and are the most linear waves. This agreement is seen in both the rear and starboard line. For the larger sea states, the error for Configurations 1 begins to increase significantly. For the considered sea states, it is not possible to show results for these two configurations for the sea states with frequencies lower than 0.1 Hz (the extreme sea states). Under these conditions, the motions became so large that the solver could not find a solution. The largest error is found for the sea states with peak frequencies around 0.12 Hz. Considering the tested sea states in Figure 7, these sea states also correspond to the steepest sea states. Still, the maximum deviation for Configuration 2 is 26% for the $T_{MPM}$ for the rear line, while it is only 11% for the starboard line.

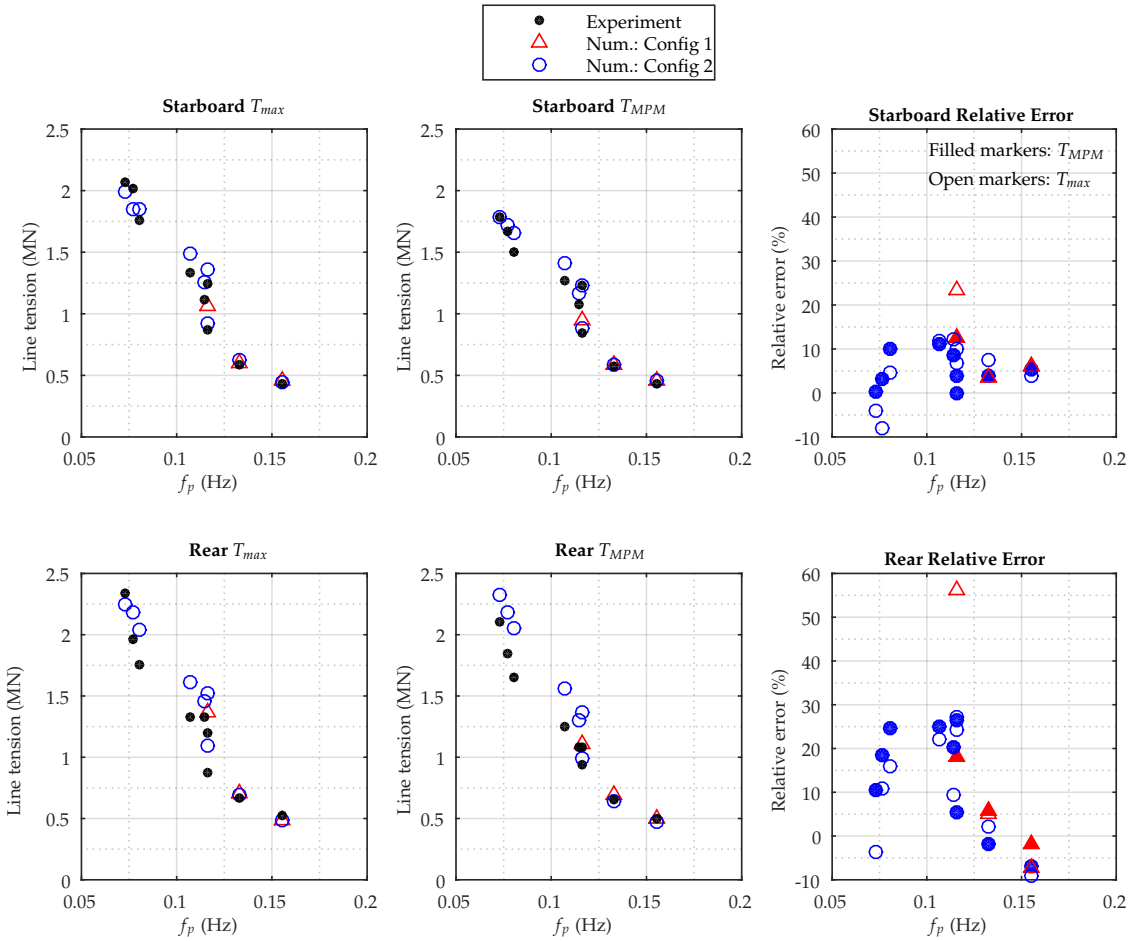


**Figure 15.** Comparison of extreme tensions for the irregular sea states.

The extreme motion of the device is also of interest, and the results are plotted in Figure 16. Despite the good agreement seen in the previous figure, a larger deviation is found. The numerical model particularly overestimates the pitch motion. Even though some quadratic damping is added in the pitch DoF, it still appears that more damping is needed. For Configuration 1, the relative error exceeds 100%, with a maximum of 150%. The drag element in Configuration 2 decreases the error to a maximum of 78%, which is still a significant overestimation. The smallest error is found for the operational sea conditions in deep water, with a smaller wave steepness.

The surge motion is overestimated with a maximum of 32% in the most extreme situation. This sea state is also the sea state in most shallow water and, according to Figure 7, also the sea state where the diffraction contribution is smallest and drag and inertia most important. The surge maximums are underestimated for the sea states with the highest frequency.

The heave motion causes the smallest relative error, with a maximum absolute value of 27%.

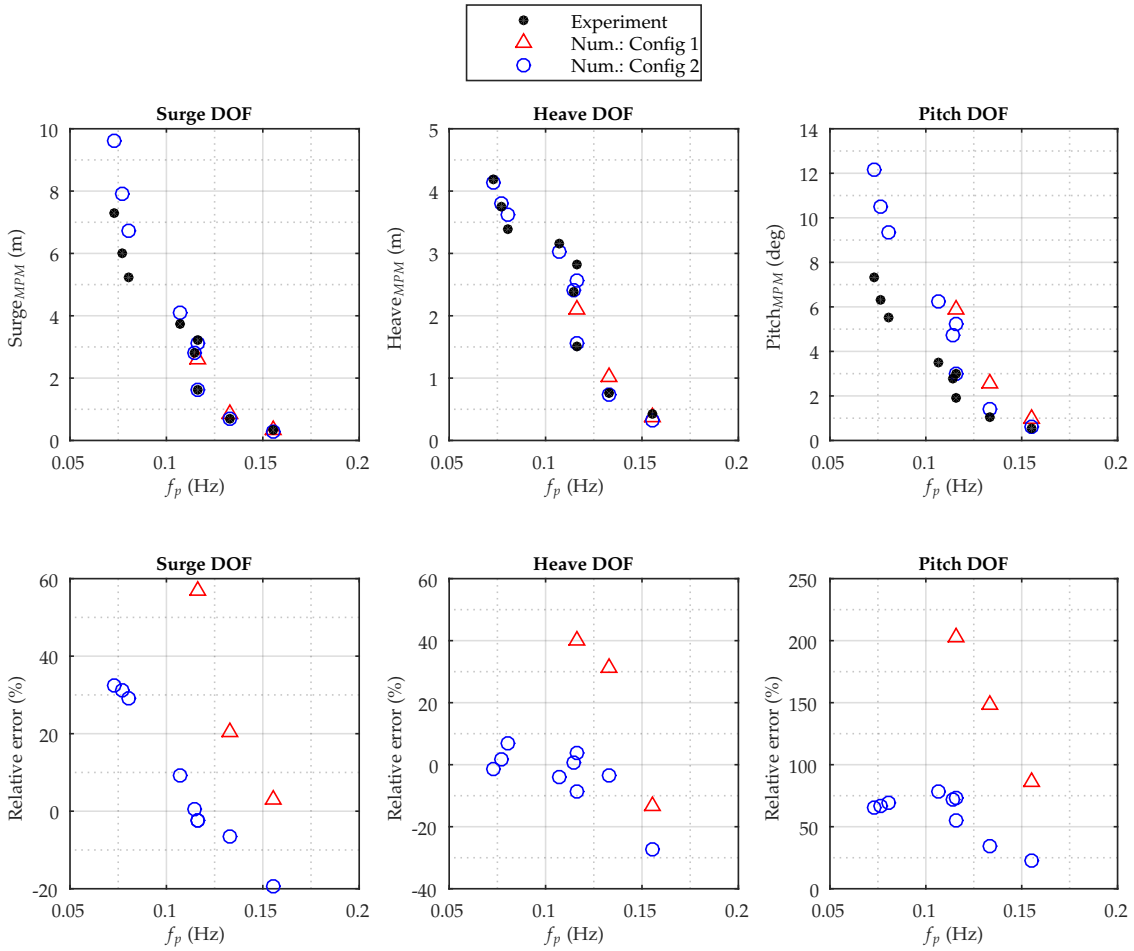


**Figure 16.** Comparison of extreme motions for the irregular sea states.

### 3.5. Optimized Model

As stated previously, the objective of this paper is to validate that a numerical model can be used in an initial design procedure, where no experimental data are available for optimization and tuning of the model. The results presented in the previous sections indicate that the structure can be modeled with some overestimation of response compared to the experiments. Considering Figure 9, the deviation appears to be caused by especially insufficient damping. Some quadratic damping has been added by the drag element, but the figure showed significant underestimation of the linear damping. Figure 17a illustrates a decay test where 370 $\frac{\text{kN}}{\text{m/s}}$ linear damping has been added in surge.

The additional damping clearly results in a better agreement between the surge motion in the experiment and model, which is also illustrated in Figure 17b, where the linear regression now indicates a minor difference between both linear and quadratic damping. For the optimized model, the additional linear damping results in a coefficient $p_1 = 0.0171$ s$^{-1}$, which corresponds to a relative error of 4.3% from the experiments.

Since no decay tests are available for heave and pitch, it is more difficult to tune these values. The work in [13] presented a method that can be used, but the present study made a coarse sensitivity analysis to find values of linear damping in heave and pitch, which improves the model results for the regular tests. By adding 1000 $\frac{\text{kN}}{\text{m/s}}$ and 4000 $\frac{\text{kNm}}{\text{rad/s}}$ in respectively heave and pitch, the model showed better agreement with experiments. Figure 18 presents the motion RAOs for the optimized model. Clearly, the figure indicates that the additional linear damping is the main cause of difference between Configuration 2 and the experiments. By adding the damping, also the mean drift is better estimated.

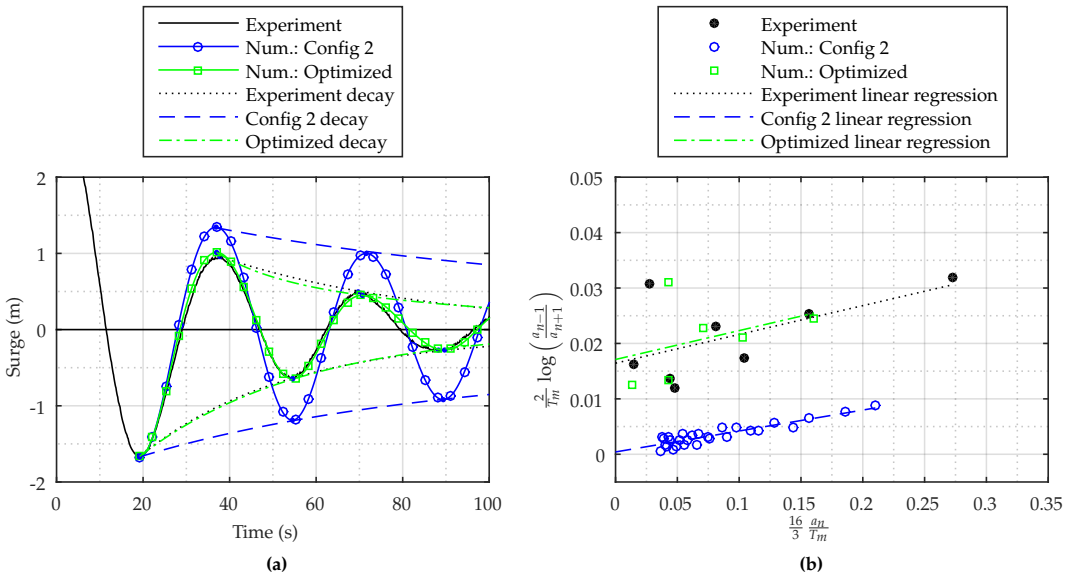


**Figure 17.** (**a**) Decay test from experiments, the model with drag elements (Configuration 2) and the optimized model with additional linear damping; (**b**) determination of $p_1$ and $p_2$ from the experiments, Configuration 2 and the optimized model using linear regression.

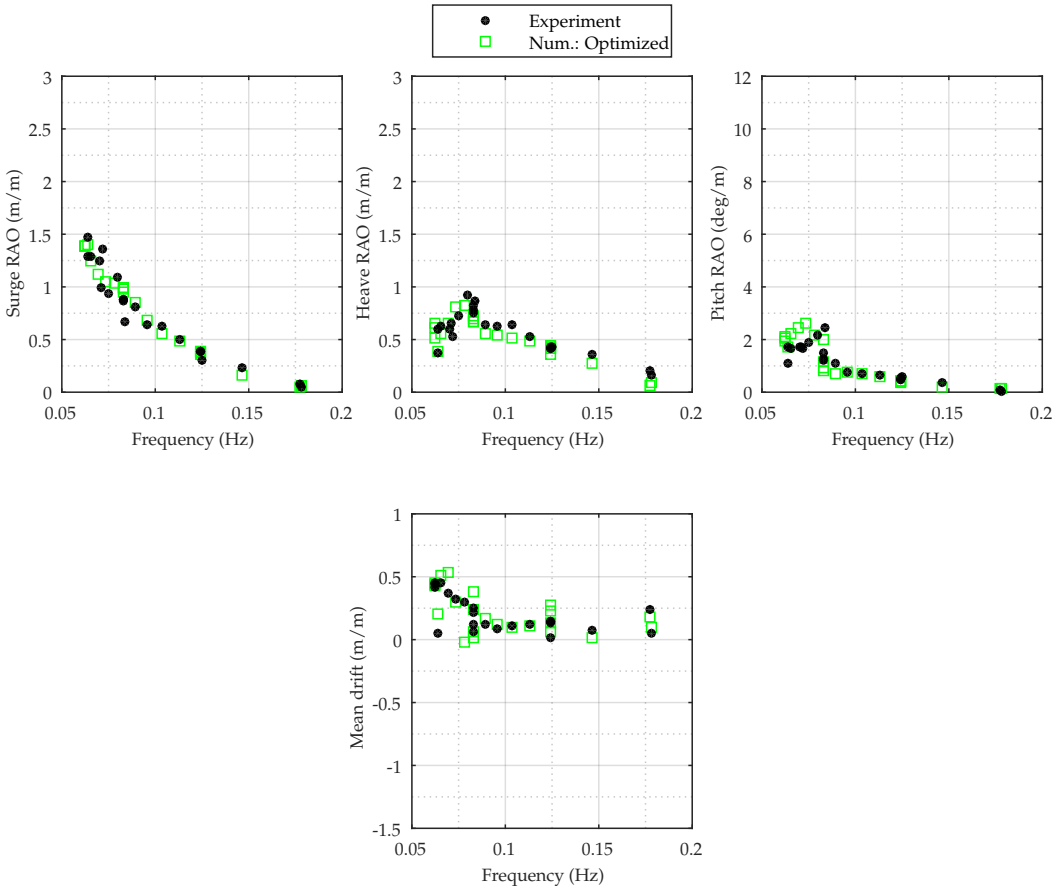


**Figure 18.** Comparison of the optimized numerical model with experimental data for all regular sea states.

The results clearly indicate the importance of tuning the model. This, however, requires the use of experiments, and as mentioned, this is not always available in initial design. The quadratic damping in this study has been added based on the geometry of the device and not experimental data, and therefore, Configuration 2 resembles a model that can be used initially to analyze the mooring system before a final solution is chosen, experimental data or more sophisticated models are produced and the numerical model is optimized.

## 4. Discussion

This study has used a large set of experimental data to validate a numerical model to be used in the initial design of mooring systems. It has been attempted to ensure similarity between model and laboratory in order to compare results, but sources of error are present during experiments. As stated previously, a small scale of 1:64.5 puts high demands on measurement precision, model manufacturing, anchor positioning, etc., and even minor uncertainties on measurements have high influence on the full-scale values. Similarly, in some of the tests, e.g., the quasi-static test, the model was displaced manually, which eventually will introduce some inaccuracy. The wave basin at Aalborg University is equipped with a passive absorber, and the maximum reflection during the test campaign was approximately 20% for the longest waves. The reflective waves were not modeled in the numerical model and could provide some divergence between model and experiment. Finally, it must also be mentioned that the anchors used in the test campaign were relatively large (cf. Figure 5) and could potentially have influenced the wave field around the model, at least for the longest waves. During the tests, it was attempted to minimize the influence of all sources of error, and hence, they are assumed not to affect the reliability of the results.

A quasi-static test was performed (cf. Figure 8) for validation of the static behavior of the numerical model, its capability of modeling the mooring tension and stiffness and the mooring layout. Good agreement was seen and proved that a good resemblance between the numerical and experimental layout was present and that the defined stiffness of the lines had been achieved. This was additionally seen from the decay test in Figure 9. Close values of the surge natural frequency were achieved, also indicating that the calculation of added mass was correct. Due to the complex geometry, it was not possible to generate reliable decay tests for heave and pitch without activating more than one DoF at a time. The added mass can also affect the natural frequencies, but since it is also indicated to be modeled correctly in surge, it is expected to show similar results in heave and pitch. Considering the behavior found in the dynamic tests, this seems to be correct.

The decay highlighted a significant underestimation of the damping in the numerical model, both for linear and quadratic damping. By adding a drag element, the error of the quadratic damping was decreased, but naturally, the linear damping still showed a significant error. Considering the difference in Figure 9 and the influence of adding a drag element, it is clear that CFD simulations and experiments are needed in order to determine drag coefficients and produce a better model of the system. This was out of scope of this study, but is crucial to consider before a final mooring design can be achieved. The underestimation of linear damping in the model was illustrated in Figures 17 and 18, where additional damping had been added and better agreement was found for the RAOs and drift motion. A potential source of this error is the presence of the thin heave damper plates in the model, which need to be solved using either a very fine mesh or a thin plate approximation, which is not included in the present version of NEMOH. This capability is included in other software packages like WAMIT [37] and will be implemented in the next releases of NEMOH. The present study did not investigate this problem further, but its influence will be investigated in future research.

Based on a range of regular wave tests, the RAOs were defined in Figure 10. Agreement between the experimental and numerical results was found in most of the frequency range for both model configurations. Some error was seen, particularly for heave and pitch at the natural frequency, and most dominantly when no drag elements were applied. By introducing drag into the pitch and heave DoF, significantly better results were obtained. At the peak frequency, the most outspoken motions will

occur and hence put most demand on the introduction of drag, but it is also at that frequency where most stress is put on the assumptions of the linear potential wave theory, which is assuming small amplitude wave and body motions.

The drift motion showed the largest error in the model. The model uses the Newman approximation, which is known to be poor in shallower water depths and when resonant motions are present. The use of full QTFs potentially could improve the model and should be investigated in future research. The calculated drift coefficients are based on the first order results from the linear potential theory. Here, the motions are used to calculate the drift, and these are overestimated due to the lack of the drag and damping. From the optimized model in Figure 18, it is seen that by adding more damping, the motions are better described, and a similar observation can be made for the drift.

From the irregular sea states, the extreme tension and motions from experiments and numerical code were compared, and the code showed a maximum relative error of approximately 26% for the line tension. Considering that this paper focuses on the applicability of the numerical model at an initial design phase where no experimental data are available and no tuning performed, this error is within an expected and reasonable range. Based on the objective of the study, the capability of the code to model the line tensions is, therefore, validated. The motion of the device was highly overestimated in pitch and probably needs more damping than what was introduced by the drag element. This was particularly shown in Figure 17. The overestimation of extreme surge might be a result of the overestimation of drift. Despite the higher relative error of the motion, the relative error of tension was at an acceptable level.

The study has shown that a relatively reliable numerical model can be constructed and used in initial analysis to model extreme design values for mooring lines, even without tuning it to experimental data, but only adding a drag element determined by a simplified method without the use of experiments. The analysis provided an understanding of the errors and limitations, which can be taken into account in future analysis of the structures. It is expected that this approach can be used for other similar WECs as presented in a previous section. The results naturally need to be treated with caution, and the best description of the device is achieved by using experimental data to optimize the model.

Since the model overestimates loads and motions, it could be highly beneficial to tune the model to lower the loads and, thereby, decrease the need for strength of the lines. When considering that design standards like, e.g., [10] or [11] introduce safety factors in the range of 1.4–1.67, much safety is now in the system. From a survivability point of view, this can be desirable, but it will not help in reducing the cost of the moorings. For a final and complete design, it is therefore desirable to optimize the model as much as possible. For initial design, use of the model in this paper will provide usable results that can be applied in further investigation of mooring systems.

## 5. Conclusions

The present paper presented the outcome of an experimental test campaign and used the results to validate a numerical model, constructed by use of the BEM code NEMOH and the time domain mooring analysis tool OrcaFlex. Focus was put on the expected sea conditions for a specific deployment site and sea states covering the expected frequency and wave height range. This included both operational and extreme conditions. The aim of the paper was to investigate the potential of the codes to calculate the extreme response for line tension in particular and, hence, their applicability in initial mooring design for large WECs. In addition, the work presented the influence of applying drag elements with the use of simplified theory, and not laboratory or CFD results, in order to improve the BEM model. The focus was to achieve an understanding of the obtained error when considering the extreme response, in order to use the model in initial design phases where, e.g., experimental data are not available. The main error was shown to be caused by underestimation of the damping in the model. By adding a drag element without the use of experimental tuning, it was possible to improve the quadratic damping significantly, but the linear damping was still underestimated. The results are expected to be applicable

to similar devices with passive mooring and where the PTO is in safety mode during extreme events. The model showed an error that can be accepted in initial phases; however, the study highlighted the inaccuracies from parameters such as linear and quadratic damping, and these must be minimized before a complete and final mooring design can be achieved.

**Acknowledgments:** The present study was funded by the Energy Technology Development and Demonstration Program (EUDP) and its project "Mooring Solutions for Large Wave Energy Converters" (Grant Number 64014-0139). The authors wish to acknowledge the Floating Power Plant for input on the experimental work.

**Author Contributions:** J.B.T., F.F. and J.P.K. defined the outline of the study and the experimental work in a shared effort. J.B.T. mainly performed the experimental work with input from F.F. and J.P.K. J.B.T. analyzed the data and performed the numerical analysis. J.B.T. drafted the paper, while F.F. and J.P.K. provided important input and review needed for finalization of the paper.

**Conflicts of Interest:** The authors declare no conflict of interest.

## References

1. Floating Power Plant. Available online: http://www.floatingpowerplant.com/ (accessed on 5 April 2017).
2. LEANCON Wave Energy. Available online: http://www.leancon.com/ (accessed on 5 April 2017).
3. Wave Dragon. Available online: http://www.wavedragon.net/ (accessed on 5 April 2017).
4. Cruz, J. *Ocean Wave Energy: Current Status and Future Perspectives*; Springer: Berlin, Germany, 2008.
5. Martinelli, L.; Ruol, P.; Cortellazzo, G. On mooring design of wave energy converters: The Seabreath application. *Coast. Eng. Proc.* **2012**, *1*, doi:10.9753/icce.v33.structures.3.
6. Fitzgerald, J. Position Mooring of Wave Energy Converters. Ph.D. Thesis, Chalmers Univerisity of Technology, Goteborg, Sweden, 2009.
7. Thomsen, J.; Kofoed, J.; Delaney, M.; Banfield, S. Initial Assessment of Mooring Solutions for Floating Wave Energy Converters. In Proceedings of the Twenty-Sixth (2016) International Ocean and Polar Engineering Conference, Rhodes, Greece, 26 June–2 July 2016; Chung, J., Muskulus, M., Kokkinis, T., Wang, A., Eds.; International Society of Offshore & Polar Engineers: Cupertino, CA, USA, 2016; Volume 1, pp. 590–596.
8. Ridge, I.; Banfield, S.; Mackay, J. Nylon fibre rope moorings for wave energy converters. In Proceedings of the OCEANS 2010, Seattle, WA, USA, 20–23 September 2010; pp. 1–10.
9. Fitzgerald, J.; Bergdahl, L. Considering mooring cables for offshore wave energy converters. In Proceedings of the 7th European Wave and Tidal Energy Conference, Porto, Portugal, 11–14 September 2007.
10. Det Norske Veritas (DNV). *Position Mooring*; DNV Offshore Standard DNV-OS-E301; DNV: Høvik, Norway, 2010.
11. API. *Design and Analysis of Stationkeeping Systems for Floating Structures*; American Petroleum Institute API-RP-2SK; API: Washington, DC, USA, 2005.
12. ISO. *Stationkeeping Systems for Floating Offshore Structures and Mobile Offshore Units*; ISO 19901-7:2005; ISO: Geneva, Switzerland, 2013.
13. Harnois, V.; Weller, S.D.; Johanning, L.; Thies, P.R.; Le Boulluec, M.; Le Roux, D.; Soule, V.; Ohana, J. Numerical model validation for mooring systems: Method and application for wave energy converters. *Renew. Energy* **2015**, *75*, 869–887.
14. Andersen, M.T.; Wendt, F.F.; Robertson, A.N.; Jonkman, J.M.; Hall, M. Verification and Validation of Multisegmented Mooring Capabilities in FAST v8. In Proceedings of the 26th International Ocean and Polar Engineering Conference, Rhodes, Greece, 26 June–2 July 2016; International Society of Offshore and Polar Engineers: Cupertino, CA, USA, 2016.
15. Wendt, F.F.; Andersen, M.T.; Robertson, A.N.; Jonkman, J.M. Verification and Validation of the New Dynamic Mooring Modules Available in FAST v8. In Proceedings of the 26th International Ocean and Polar Engineering Conference, Rhodes, Greece, 26 June–2 July 2016; International Society of Offshore and Polar Engineers: Cupertino, CA, USA, 2016.
16. Oberkampf, W.L.; Trucano, T.G. Verification and validation in computational fluid dynamics. *Prog. Aerosp. Sci.* **2002**, *38*, 209–272.
17. Babarit, A.; Delhommeau, G. Theoretical and numerical aspects of the open source BEM solver NEMOH. In Proceedings of the 11th European Wave and Tidal Energy Conference (EWTEC2015), Nantes, France, 6–11 September 2015.

18. Orcina Ltd. *Orcaflex User Manual*; Orcina Ltd.: Cumbria, UK, 2013.
19. Thomsen, J.; Ferri, F.; Kofoed, J. Experimental testing of moorings for large floating wave energy converters. In *Progress in Renewable Energies Offshore*; Soares, C., Ed.; CRC Press LLC: Boca Raton, FL, USA, 2016; pp. 703–710.
20. *Assessment of Mooring System for Marine Energy Converters (MECs)*; IEC 62600-10; International Electrotechnical Commission (IEC): Geneva, Switzerland, 2014.
21. DNV. *Design of Floating Wind Turbine Structures*; DNV Offshore Standard DNV-OS-J103; DNV: Høvik, Norway, 2013.
22. Wehmeyer, C.; Ferri, F.; Andersen, M.T.; Pedersen, R.R. Hybrid Model Representation of a TLP including flexible topsides in non-linear regular waves. *Energies* **2014**, *7*, 5047–5064.
23. Hall, M.; Goupee, A. Validation of a lumped-mass mooring line model with DeepCwind semisubmersible model test data. *Ocean Eng.* **2015**, *104*, 590–603.
24. Subrata, K.C. *Handbook of Offshore Engineering*; Elsevier Science: Amsterdam, The Netherlands, 2005.
25. Newman, J.T. The drift force and moment on ships in waves. *J. Ship Res.* **1967**, *11*, 51–60.
26. Ecole Centrales Nantes. Available online: http://lheea.ec-nantes.fr/doku.php/emo/nemoh/start (accessed on 5 April 2017).
27. Newman, J. Second-order, slowly-varying forces on vessels in irregular waves. In Proceedings of the International Symposium on the Dynamics of Marine Vehicles and Structures in Waves, London, UK, May 1974.
28. DNV. *Environmental Conditions and Environmental Loads*; DNV Recommended Practice DNV-RP-C205; DNV: Høvik, Norway, 2014.
29. AwaSys 7. Two and Three Dimensional Wave Generation, 2016. Available online: http://www.hydrosoft.civil.aau.dk/awasys/ (accessed on 5 April 2017).
30. WaveLab 3. Data Acquisition and Analysis Software. Department of Civil Engineering, Aalborg University, 2016. Available online: http://www.hydrosoft.civil.aau.dk/wavelab/ (accessed on 5 April 2017).
31. OptiTrack. Motion Capture Systems. NaturalPoint, Inc., 2016. Available online: https://www.optitrack.com/ (accessed on 5 April 2017).
32. Ingram, D.; Smith, G.; Bittencourt-Ferreira, C.; Smith, H. *Protocols for the Equitable Assessment of Marine Energy Convertes*; Technical Report; University of Edinburgh: Edinburgh, UK, 2011; ISBN 978-0-9508920-2-3.
33. McCombes, T.; Johnstone, C.; Holmes, B.; Myers, L.; Bahaj, A.; Heller, V.; Kofoed, J.; Finn, J.; Bittencourt, C. *Assessment of Current Practice for Tank Testing of Small Marine Energy Devices*; Technical Report, EquiMar Deliverable; Aalborg University: Aalborg, Denmark, 2010.
34. Bridon. Wire and Fibre Rope Solutions, 2016. Available online: http://www.bridon.com/uk/ (accessed on 5 April 2017).
35. Le Mehaute, B. *An introduction to Hydrodynamics and Water Waves*; Springer Science & Business Media: New York, NY, USA, 1976.
36. Faltinsen, O. *Sea Loads on Ships and Offshore Structures*; Cambridge University Press: Cambridge, UK, 1993; Volume 1.
37. Lee, C.H.; Newman, J.N. *WAMIT User Manual*; WAMIT, Inc.: Chestnut Hill, MA, USA, 2016.